Research Square

Preprints are preliminary reports that have not undergone peer review.
They should not be considered conclusive, used to inform clinical practice,
or referenced by the media as validated information.

# Multi-decadal trends in SST, chlorophyll-a, NPP and atmospheric forcing across oligotrophic and upwelling regions of the Northeast Atlantic

**Charlotte Pereira**
Centro Oceanográfico de Canarias, Instituto Español de Oceanografía, Consejo Superior de Investigaciones Científicas (IEO-CSIC)

**Alba González-Vega**
Centro Oceanográfico de Canarias, Instituto Español de Oceanografía, Consejo Superior de Investigaciones Científicas (IEO-CSIC)

**Francisco Machín**
Universidad de Las Palmas de Gran Canaria

**Eduard Puig-Montellà**
Centro Oceanográfico de Canarias, Instituto Español de Oceanografía, Consejo Superior de Investigaciones Científicas (IEO-CSIC)

**Juan Pablo Martín-Díaz**
Centro Oceanográfico de Canarias, Instituto Español de Oceanografía, Consejo Superior de Investigaciones Científicas (IEO-CSIC)

**Sarah Ayuso-Candal**
Centro Oceanográfico de Canarias, Instituto Español de Oceanografía, Consejo Superior de Investigaciones Científicas (IEO-CSIC)

**Eugenio Fraile-Nuez**
eugenio.fraile@ieo.csic.es

Centro Oceanográfico de Canarias, Instituto Español de Oceanografía, Consejo Superior de Investigaciones Científicas (IEO-CSIC)

**Article**

**Keywords:** Climate Change, Linear trends, Subtropical Gyre, Upwelling, Northeast Atlantic Ocean

**Posted Date:** November 16th, 2026

**DOI:** https://doi.org/10.21203/rs.3.rs-10727918/v1

**License:** This work is licensed under a Creative Commons Attribution 4.0 International License.
Read Full License

**Additional Declarations:** No competing interests reported.

# Multi-decadal trends in SST, chlorophyll-*a*, NPP and atmospheric forcing across oligotrophic and upwelling regions of the Northeast Atlantic

**Charlotte Pereira[1], Alba González-Vega[1], Francisco Machín[2], Eduard Puig Montellà[1], Juan Pablo Martín-Díaz[1,3], Sarah Ayuso-Candal[1] and Eugenio Fraile-Nuez[1]***

[1]Centro Oceanográfico de Canarias, Instituto Español de Oceanografía, Consejo Superior de Investigaciones Científicas (IEO-CSIC), 38180 Santa Cruz de Tenerife, Spain.

[2]Departamento de Física, Universidad de Las Palmas de Gran Canaria, 35017 Las Palmas de Gran Canaria, Spain.

[3]Universidad de La Laguna (ULL), 38200 San Cristóbal de La Laguna, Spain.

*Corresponding author: Eugenio Fraile-Nuez (eugenio.fraile@ieo.csic.es)

**Key Words:**

- Climate Change
- Linear trends
- Subtropical Gyre
- Upwelling
- Northeast Atlantic Ocean

## Abstract

Climate change is reshaping the Northeast Atlantic, yet its impact differs between oligotrophic and upwelling ecosystems. We analysed multi-decadal trends from satellite and reanalysis datasets of sea surface temperature (SST), chlorophyll-*a* (chl-*a*), net primary production (NPP), and wind stress across the Northeast Atlantic Subtropical Gyre and adjacent upwelling regions. SST increased across the region, with the strongest warming in the Azores (+3.18 °C century$^{-1}$) and the weakest in the Permanent Upwelling (PU) region (+1.37 °C century$^{-1}$). Chl-*a* trends were predominantly negative, with the largest decline in PU (−1.62 mg m$^{-3}$ century$^{-1}$), accompanied by a reduction in highly productive area (−6.25 % century$^{-1}$). NPP also declined, with the strongest trends in the Cape Juby Weak Permanent Upwelling and Seasonal Upwelling region (−459.56 and −351.38 mg C m$^{-2}$ day$^{-1}$ century$^{-1}$, respectively). Upwelling-favourable wind stress intensified in the Northwest African upwelling system, reaching +15.98 mN m$^{-2}$ century$^{-1}$ in PU and +12.32 mN m$^{-2}$ century$^{-1}$ in Cape Juby, but without increased chl-*a* concentrations. Comparison with trends ending in 2019 indicated stronger SST and chl-*a* trends, suggesting that the 2023–2024 North Atlantic marine heatwave influenced warming estimates.


## 1 Introduction

Climate change is driving widespread physical and biogeochemical alterations in the state of the global ocean. Surpassing 1.5 °C of global mean temperature anomaly could trigger multiple climate tipping points, including ice-sheet destabilization and widespread coral reef degradation [1]. Although the Intergovernmental Panel on Climate Change projected this threshold would be reached in the early 2030s under most scenarios [2], recent data indicate that global average temperatures have already exceeded it, reaching 1.6 °C above pre-industrial levels [3].

More than 90% of the excess heat is stored within oceans [4-8], warming surface and deep layers [9-11]. Rising sea surface temperature (SST) alters oceanic and atmospheric circulation, strengthens stratification, reduces vertical mixing and nutrient upwelling, and disrupts marine ecosystems [12-16].

Multiple studies have shown that the global signal of ocean warming over recent decades has been accompanied by a declining trend in chlorophyll-*a* [17-21], indicating negative impacts on phytoplankton. As phytoplankton contribute roughly half of global net primary production (NPP) and play a key role in carbon cycling and marine food webs [22-24], their decline has major ecological consequences, including shifts in species distribution and increased extinction risk [14,17,25,26]. In addition, most equatorial regions, subtropical gyres and hotspots have experienced some of the strongest chlorophyll declines [20,27].

Subtropical gyres are large, anticyclonic oceanic systems covering approximately 40-60% of the global ocean. Their warm, highly stratified, and nutrient-poor waters lead to low chlorophyll-*a* (chl-*a*) concentrations and NPP, though their sheer size makes them key contributors to global ocean productivity [20,28-30]. Their circulation is primarily driven by wind

stress [31-32]. Consequently, changes in atmospheric circulation can redistribute heat and water masses and impact regional sea levels [33]. The oligotrophic regions of the North Pacific and North Atlantic gyres have expanded significantly, whereas Southern Hemisphere gyres display weaker trends [29]. Several studies also report increasing SST and declining chl-*a* and NPP in the North Atlantic Subtropical Gyre [19,30,34-36].

Eastern Boundary Upwelling Systems (EBUSs) are sustaining 20% of global fisheries production despite occupying only 1% of the ocean surface [37,38]. However, climate change impacts on EBUSs remain uncertain since observations are contradictory: major upwelling systems have shown an increase in SST [39-40], whereas upwelling-favourable winds and chl-*a* have increased in most EBUSs [41-43]. Although recent increases in meridional wind intensity have been reported in the Canary Upwelling System, declining chl-*a* is still observed [19] This upwelling system is mainly driven by the Azores High as it provides winds parallel to the coast, enabling the Ekman transport. However, most models suggest a poleward displacement of the Azores High [44-47] due to climate change, as well as an increase in air pressure (intensification) in its centre [48], enhancing upwelling off the Iberian Peninsula [43,49,50]. These changes may extend the upwelling season in the north while weakening in the south [44,50]. Some studies already report declining upwelling intensity, chl-*a*, NPP and equatorward winds in the Canary Upwelling System [39,51,52].

This study estimates climate trends of SST, chl-*a*, wind, and NPP in the Eastern North Atlantic subtropical gyre (NASE) region. Satellite products with high spatial and temporal resolution of SST, chl-*a*, NPP, and meridional wind will be used for this study. While retaining the regional framework of Siemer et al. (2021) [19] to ensure comparability, this study introduces a finer subdivision of the Azores, Madeira and Canary archipelagos to distinguish open-ocean, island and coastal upwelling waters, allowing the identification of regional patterns that may be obscured when averaging over larger areas. In recent years, several extreme meteorological events have occurred in the North Atlantic region, including the 2023–2024 marine heatwave, record-breaking atmospheric and sea surface temperatures in 2024, and multiple episodes of intense precipitation [53-56]. These events may have had an influence on oceanic and atmospheric dynamics, possibly altering some of the calculated trends. Because these events occur at the end of the observational record, they may substantially influence the estimation of long-term linear trends and reveal possible non-linear behaviour. Therefore, trends ending in 2019 and 2025 are compared to assess their sensitivity to these extreme events and potential non-linear behaviour.

## 2 Results

### 2.1 SST

Mean SST anomaly time series and their linear trends for each box are shown in Figure 2. All regions exhibit positive SST trends, with the steepest slopes in the oceanic boxes, particularly

around the Azores. All time series display a marked SST peak from 2024 onwards, associated with the 2023–2024 Northeast Atlantic marine heatwave.

Figure 2a shows the spatial distribution of SST anomaly trends across the NASE region for 1982–2025 (44 years). Table 2 summarizes mean SST trends and their statistical significance for all study boxes and compares the 1982-2019 and 1982-2025 periods to assess the influence of recent years on estimated warming rates.

Positive trends dominate the study area, including EBUSs, except for localized cooling in PU and CGWPU reaching −2.00 °C century$^{-1}$. The strongest warming occurs in the Azores (AZ; +3.18 °C century$^{-1}$, $p < 0.05$, Table 2) peaking in the eastern waters (AZ3; +3.39 °C century$^{-1}$; $p<0.05$), whereas the westernmost islands (AZ1) warms slower. In Madeira, coastal waters (MA1) warm faster than adjacent open-ocean waters (MA2). In the Canary Islands, the mean trend (CI) reaches +2.45 °C century$^{-1}$ ($p < 0.05$), with the highest warming in the upwelling filament and eddy region (CI3; +2.47 °C century$^{-1}$; $p < 0.05$), and the lowest in the easternmost islands (CI2; +2.38 °C century$^{-1}$; $p < 0.05$).

EBUSs generally display weaker warming, ranging from +1.37 °C century$^{-1}$ in PU to +2.02 °C century$^{-1}$ in SU ($p < 0.05$). For 1982–2019, CJWPU exhibits both the weakest warming (+0.90 °C century$^{-1}$; $p < 0.05$) and the largest increase relative to the 1982–2025 estimate among the upwelling regions.

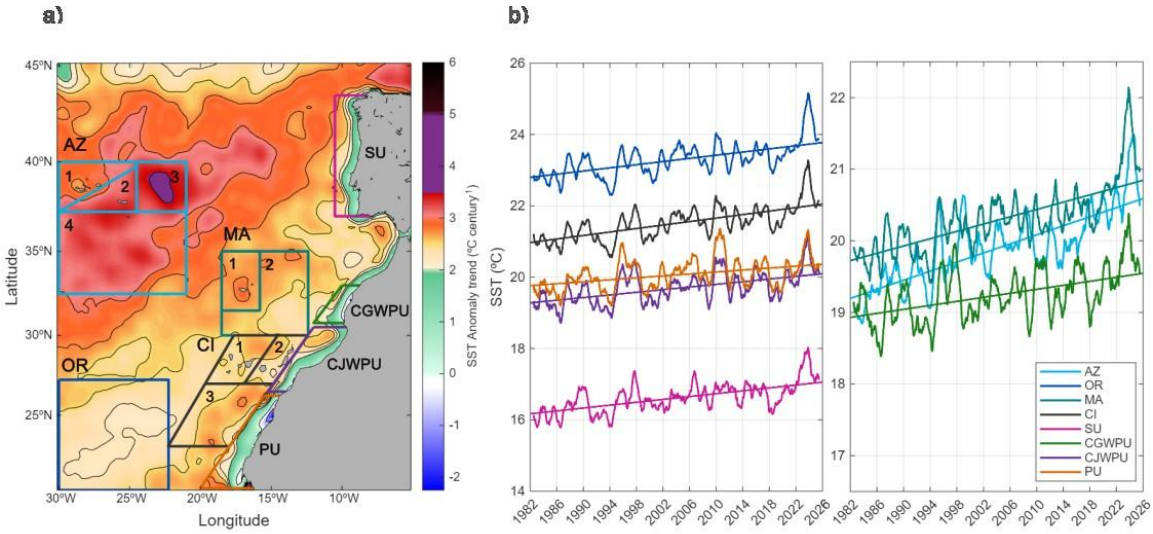



**Figure 2.** (**a)** Spatial distribution of trends in sea surface temperature anomalies in the NASE region (1982–2025). Negative trends are shown in blue and near zero trends in white. The boundaries of each subregion are indicated. **(b)** Smoothed mean SST time series (366 days moving average) for each region. Trends were calculated from anomaly time series, to which the

corresponding mean values were added back for visualization purposes only. Trends are separated into two plots for better visualization to avoid overlapping.

### 2.2 Chl-*a*

Figure 3 shows the spatial distribution of surface chlorophyll-*a* concentration anomaly trends for 1998–2025. Negative trends dominate the study region, especially nearshore and in the open ocean north of 32°N, whereas positive trends occur in the Canary and Madeira archipelagos, south of 32°N, and locally along the western Iberian coast. EBUSs exhibit the largest rates of change. All upwelling boxes show declining chl-*a*, with PU showing the strongest drop ($-1.62$ mg $m^{-3}$ $century^{-1}$; $p < 0.05$, Table 2). Oceanic regions display trends close to zero, with the Madeira subregion presenting the weakest trends, with only MA1 being significant (-0.003 mg $m^{-3}$ $century^{-1}$; $p< 0.05$). In the Azores, all subregions exhibit negative trends, strongest in the eastern islands and waters east of the archipelago ($-0.07$ and $-0.10$ mg $m^{-3}$ $century^{-1}$; $p < 0.05$).

Figure 3b shows the mean chlorophyll-*a* time series and linear trends for each mean box. PU, CI, and AZ, exhibit high variability in surface chl-*a* anomaly, although variability decreases markedly after late 2015. In PU, chl-*a* remains below the climatological mean thereafter. Except for AZ, all open-ocean boxes show weak positive regression slopes.

Trends in the annual number of productive days (for upwelling areas) and unproductive days (open-ocean areas) are not statistically significant in any subregion, indicating insufficient evidence to support either an increase or a decrease in the number of productive/unproductive days per year, except for the PU which displays a decline of -0.27 productive days $year^{-1}$ ($p < 0.05$), and AZ1, with an increase of 0.25 desert days $year^{-1}$ ($p < 0.05$).

Open-ocean subregions, except the Azores, show declining percentages of desert area, indicating a decrease in the coverage of oligotrophic waters. The largest decrease occurs in MA2 ($-20.47$ % of desert area $century^{-1}$). Conversely, the Azores exhibit a mean expansion of

oligotrophic waters (+16.98 % century$^{-1}$), strongest in the southern and eastern subregions (+17.93 and +26.29 % century$^{-1}$, respectively).

Except for SU and CGWPU, where trends are not significant (Table 2), all EBUSs show declining highly productive area, with the largest decrease in PU (−6.25 % century$^{-1}$).

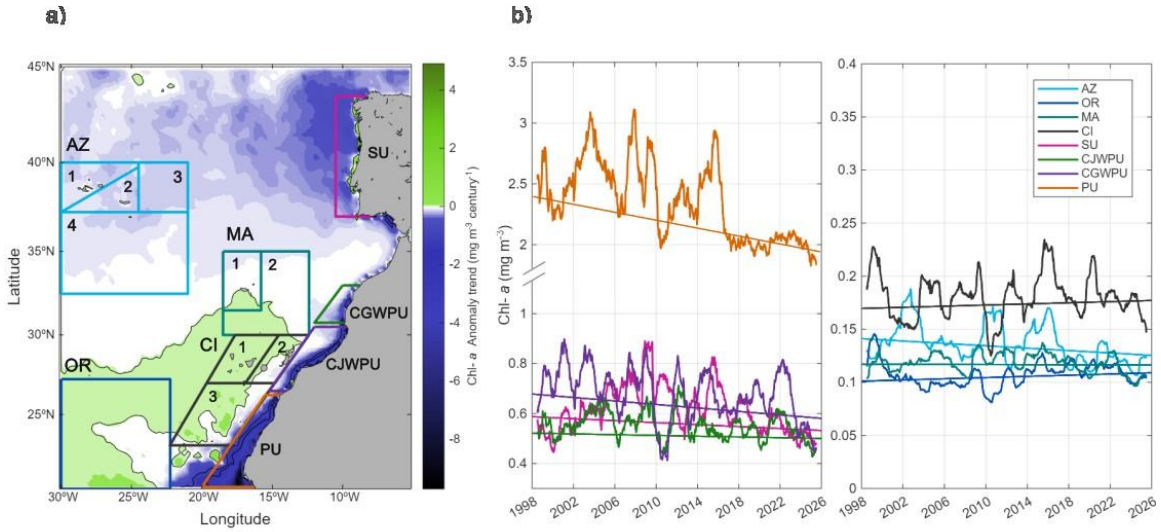



**Figure 3. (a)** Spatial distribution of trends in surface chlorophyll-*a* concentration anomalies in the NASE region (1998–2025). Negative trends are shown in blue and positive trends in green. The boundaries of each subregion are indicated. **(b)** Smoothed mean surface chl-*a* concentration time series (366 days moving average) for each subregion. Trends were calculated from anomaly time series to which the corresponding mean values were added back for visualization purposes only. Trends are separated into two plots for better visualization to avoid overlapping.

### 2.3 NPP

Figure 4 shows the spatial distribution of net primary production anomaly trends for 2003–2023. Most of the study area is characterized by predominantly negative NPP trends, with the largest declines along the North African coast, reaching −2500 mg m$^{-2}$ day$^{-1}$ century$^{-1}$ and surpassing these values locally in CJWPU. Offshore, PU exhibits strong spatial heterogeneity, with adjacent positive and negative trends that partly compensate each other, so its positive mean trend reflects a regional average rather than a uniform increase in productivity.

The westernmost box of the Azores (AZ1) show a slight increase in NPP, whereas the eastern islands (AZ2) display a decline. Weak positive trends are also observed around the western Canary Islands (CI1), with stronger increases south of the archipelago (CI3) and in OR. In SU, positive trends exceeding +2000 mg m$^{-2}$ day$^{-1}$ century$^{-1}$ occur near the Tagus River mouth,

although most of the region exhibits a significant decline (−351.38 mg $m^{-2}$ $day^{-1}$ $century^{-1}$; $p < 0.05$).

Figure 4b shows the mean temporal series of NPP for each subregion. Upwelling regions show the greatest variability, while among the open-ocean boxes only AZ and OR exhibit significant trends (Table 2).

Overall, NPP trends are predominantly negative, except in PU, CI and OR, although most CI trends are not significant. PU shows the largest increase (+362.42 mg $m^{-2}$ $day^{-1}$ $century^{-1}$; $p < 0.05$), whereas CJWPU exhibits the strongest decline (−459.56 mg $m^{-2}$ $day^{-1}$ $century^{-1}$; $p < 0.05$), followed by SU.

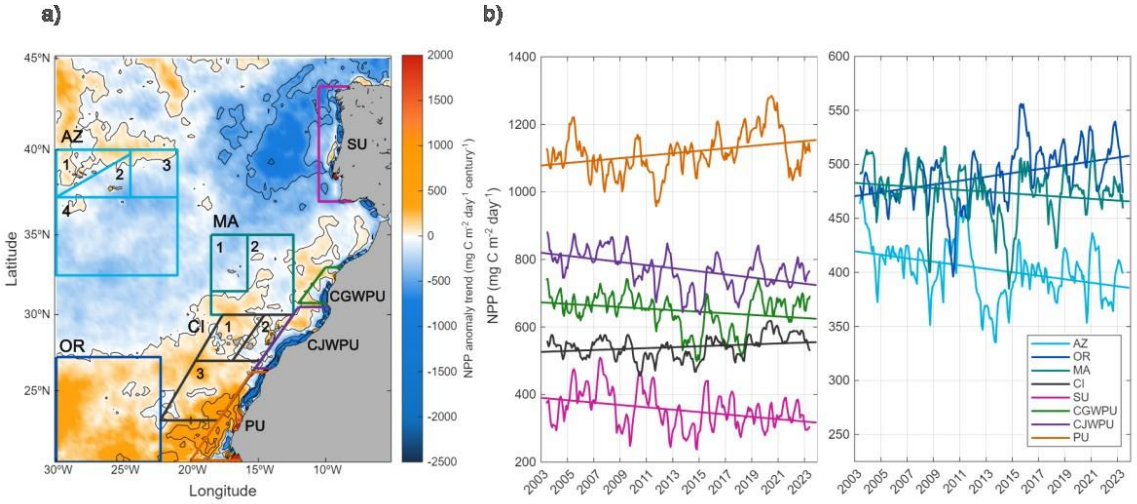



**Figure 4. (a)** Spatial distribution of trends in NPP anomalies in the NASE region (2003–2023). Negative trends are shown in blue and positive trends in orange. The boundaries of each subregion are indicated. **(b)** Smoothed mean NPP time series (12 months moving average) for each subregion. Trends were calculated from anomaly time series to which the corresponding mean values were added back for visualization purposes only. Trends are separated into two plots for better visualization to avoid overlapping.

### 2.4 Wind

Figure 5 shows the spatial distribution of meridional wind stress anomaly trends for 1992 to 2025. Because meridional wind stress is predominantly negative throughout the year (i.e., equatorward winds), negative trends indicate intensification of upwelling-favourable winds, whereas positive trends indicate weakening.

As this analysis focuses on upwelling-favourable winds, only PU, CJWPU, CGWPU, SU and CI are considered, the latter because of the influence of coastal upwelling filaments.

Unlike SU, which exhibits a weakening trends (i.e., a reduction in equatorward meridional wind stress), the remaining African upwelling regions show predominantly negative trends,

indicating a strengthening in equatorward wind stress. Around the Canary Islands, positive trends are mainly confined to the western islands, indicating a decrease in equatorward winds.

Figure 5b shows the mean time series and trends of upwelling-favorable wind stress intensity. For the calculation of these trends, except for SU, were projected onto the dominant angle between wind direction and the meridional axis in each region in order to estimate the maximum wind stress favourable for upwelling. These angles were selected under the assumption that upwelling is permanent [37], and therefore the prevailing wind corresponds to upwelling-favourable conditions. For SU, no projection was applied, as the wind is predominantly meridional and equatorward.

CGWPU exhibits the lowest variability, whereas PU shows the largest seasonal variability and the strongest trend (+15.98 mN $m^{-2}$ $century^{-1}$), followed by CJWPU (+12.32 mN $m^{-2}$ $century^{-1}$; $p < 0.05$, Table 2). No significant trends are detected in the remaining regions.

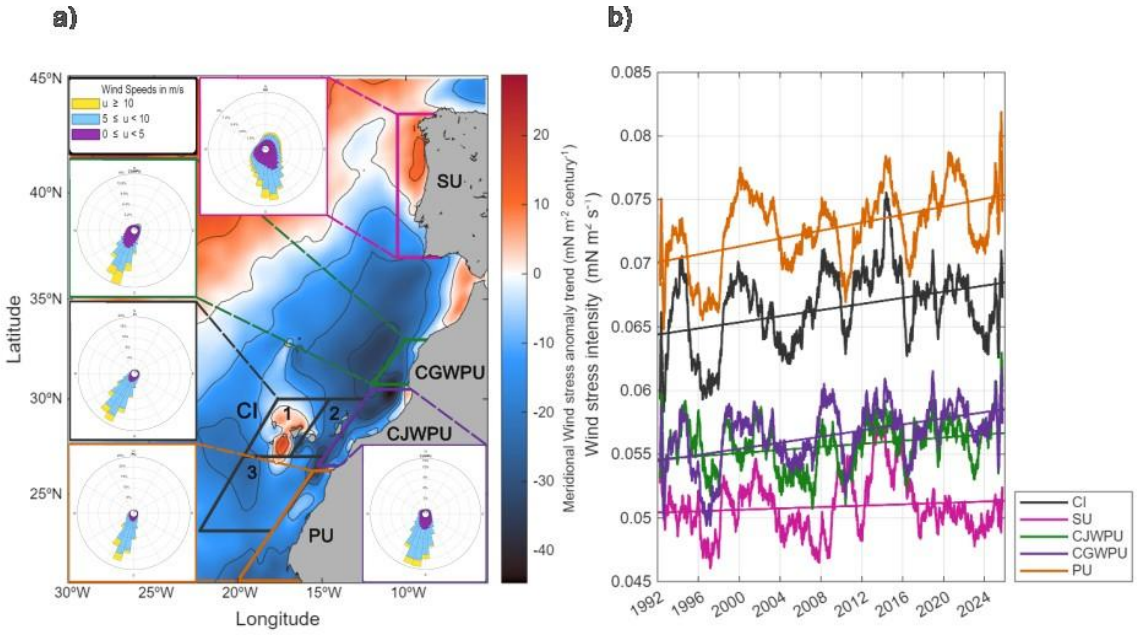



**Figure 5. (a)** Spatial distribution of trends in meridional wind anomalies in the NASE region (1992–2025). Negative trends are shown in blue and positive trends in red. The boundaries of each subregion are indicated. Wind roses are added to display the average wind distribution in each subregion. **(b)** Smoothed mean wind stress intensity time series (366 days moving average) for each subregion. In order to represent wind conditions most favourable for upwelling, data from CI, CGWPU, CJWPU, and PU were projected onto the dominant angle between wind direction and the meridional axis for each mentioned subregion. Trends were calculated from anomaly time

series to which the corresponding mean values were added back for visualization purposes only. Trends are separated into two plots for better visualization to avoid overlapping.

### 2.5 Trend estimates and effect of 2019-2025 years

Trends computed from time series ending in 2019 and 2025 are summarized in Table 2 to assess the influence of recent extreme events and potential non-linear behaviour. Clear contrasts emerge between upwelling and open-ocean regions: upwelling subregions exhibit weaker SST increases but stronger declines in surface chl-*a* and NPP.

SST trends are consistently higher for 1982–2025 than for 1982–2019. The largest differences occur in Madeira, where the warming rates increases up to +0.78 °C century$^{-1}$ when the final six years are included, whereas PU shows the smallest change (+0.16 °C century$^{-1}$; $p < 0.05$).

EBUS show higher surface chl-*a* concentrations than open-ocean areas, but also stronger long-term declines. Chl-*a* loss accelerates in the extended record, particularly in SU, where the decline strengthens by −0.47 mg m$^{-3}$ century$^{-1}$.

In open-ocean regions, desert-area trends from 1998-2025 generally become more positive, indicating faster oligotrophic expansion or a slower contraction of desert waters. OR is the main exception, shifting from oligotrophic area expansion (1998–2019) to oligotrophic area contraction (1998–2025), a change of −25.91% century$^{-1}$. Madeira shows the largest acceleration in desert expansion (+22.71% century$^{-1}$).

Among EBUSs, only CJWPU and PU exhibit significant productive-area trends in both periods. Although both continue to lose productive area, the decline weakens in the extended record, with PU changing by +3.55% century$^{-1}$.

Significant NPP trends remain negative in both periods except in OR and PU. OR retains a positive trend despite a reduction of −46.72 mg m$^{-2}$ day$^{-1}$ century$^{-1}$ (Table 2). In contrast, PU shows increasing NPP despite declining chl-*a*, with the trend strengthening by +153.47 mg m$^{-2}$ day$^{-1}$ century$^{-1}$.

CJWPU also remains negative but exhibits a marked deceleration (+434.58 mg m$^{-2}$ day$^{-1}$ century$^{-1}$). CI1, CJWPU and PU are the only subregions with significant NPP trends in both periods. Coastal wind trends remain positive but are weaker for 1992–2025 than for 1992–2019, indicating a deceleration in the intensification of upwelling-favourable winds.

## 3 Discussion

The mean SST trend for the NASE region (+2.58 °C century$^{-1}$; $p < 0.05$, Table 2) displays a stronger warming rate but remains consistent with previous estimates of +2.1 °C century$^{-1}$ for the NASE region and +2.4 °C century$^{-1}$ for the European Macaronesian region [19,57]. Earlier studies

reported lower warming rates for comparable regions, ranging from +0.5 to +1.8 °C century$^{-1}$ [20,58,59].

Lower SST trends in EBUSs are likely associated with the upwelling dynamics themselves, whereby cold waters are brought to the surface and partly buffers surface warming [60]. Accordingly, PU exhibited the weakest warming and the strongest increase in upwelling-favourable wind stress (Table 2). CJWPU likewise showed relatively weak warming and positive wind stress trends, although less pronounced than in PU. Despite this apparent intensification of upwelling, chl-*a* concentrations continue to decline in both regions. For the Canary upwelling system (CGWPU, CJWPU), other authors find stronger trends than the ones obtained in this study, spanning from +2 °C century$^{-1}$ to +5 °C century$^{-1}$ [39,61]. As for the SU subregion, some studies obtain similar results to the ones in this work [19,61,62] with values spanning from +1 °C century$^{-1}$ to +2 °C century$^{-1}$, although a higher trend of +3 °C century$^{-1}$ has also been reported for this area [63].

The strongest warming occurs in the open ocean, especially around the Azores (Figure 2). One possible explanation is that, since the core of the Azores High is located near the archipelago in summer, wind intensity is reduced [64,65], limiting the ocean's ability to release stored heat efficiently and thereby contributing to the elevated warming rates observed. In contrast, lower warming around the Canary Islands may result from both the influence of coastal upwelling and the channeling of the trade winds between the islands [66], which enhances wind speed and ocean-atmosphere heat exchange. Warming rates of approximately +2.2 °C century$^{-1}$ have been reported for the Canary region despite substantial differences in the length of the analysed records (84 and 24 years, respectively) [67,68]. These estimates are close to those obtained for the CI subregions, although the trends reported in this study are slightly higher.

It is noteworthy that all regional SST time series exhibit the signature of the 2023–2024 Northeast Atlantic marine heatwave, during which temperature anomalies reached +2.02 °C relative to the 1991–2020 mean over the North Atlantic [53,55]. Because this event occurred at the end of the study period, it likely exerts a disproportionate influence on the estimated linear trends. Accordingly, SST trends calculated for 1982–2025 are consistently higher than those ending in 2019. Previous studies have also reported an acceleration in global SST warming, from 0.6 °C century$^{-1}$ since 1900 to 2.8 °C century$^{-1}$ over the last decade [69]. Therefore, the stronger trends found here may reflect both an acceleration in ocean warming and the influence of the recent marine heatwave.

The marked differences between trends ending in 2019 and 2025 across all variables also suggest possible non-linear behaviour. Alternative approaches based on non-linear trend estimation may therefore be more appropriate, as previously proposed by other studies [70-72].

Chl-*a* anomaly trends in the EBUSs agree with previous studies, all of which reported sustained declines, although generally larger than those found here: -3.11 mg m$^{-3}$ century$^{-1}$ [19], -3.8 mg m$^{-3}$ century$^{-1}$ [51] and -5.7 mg m$^{-3}$ century$^{-1}$ [39]. Notably, the strongest SST and chl-*a*

trends were reported despite the analysis being based on the shortest record (10 years), highlighting the sensitivity of trend estimates to the study period [39].

In contrast, positive chl-*a* trends were observed in open-ocean waters off the African coast. One possible explanation is an increase in the supply of limiting nutrients through Saharan dust deposition, particularly iron, which could stimulate phytoplankton growth in these generally oligotrophic waters. However, previous studies indicate that the frequency and duration of dust intrusion events have decreased in this region, although the intensity of individual events appears to have increased, resulting in higher atmospheric dust concentrations [73,74]. In open-ocean areas, negative chl-*a* trends of approximately −0.07 and −0.09 mg $m^{-3}$ $century^{-1}$ have been reported [20]. However, more recent studies have described a positive surface chl-*a* trend of approximately +0.04 mg $m^{-3}$ $century^{-1}$ [19,57].

It is also noteworthy that the temporal trends in chl-*a* exhibit some discrepancies when compared with those observed for SST. Regions experiencing the strongest warming, such as the Azores, do not exhibit the largest declines in chl-*a*. In fact, whereas OR and CI show weak positive chl-*a* trends despite continued SST increases. Conversely, EBUSs display the weakest warming but the strongest chl-*a* declines.

As discussed previously, waters associated with the subtropical gyre are highly oligotrophic. Consequently, changes in chl-*a* concentration linked to increasing temperature may remain relatively small, which could explain the near-zero chl-*a* trends observed in regions experiencing strong SST warming. In contrast, upwelling systems appear to be more sensitive to environmental changes. In contrast, upwelling systems are naturally more productive and therefore may be more sensitive to environmental changes, resulting in stronger chl-*a* loss.

Comparison of the mean SST and chl-*a* time series (Figures 2b and 3b) further reveals that, unlike SST, the signal associated with the 2023–2024 marine heatwave is not clearly reflected in the chl-*a* records. Although reductions in surface chl-*a* are apparent in CJWPU, CGWPU and SU during this period (Figure 3b), they remain small relative to the natural interannual variability.

The spatial distribution of NPP trends (Figure 4a) generally agrees with that of chlorophyll-*a*. The largest declines in both variables occur within the EBUSs, suggesting a genuine reduction in the productive capacity of these waters. However, localized areas within PU exhibit strong positive NPP trends despite declining chl-*a*. This apparent decoupling may reflect changes in temperature and nutrient availability [75-77], photoacclimation [78-80], or shifts towards more photosynthetically efficient phytoplankton communities [81,82]. It should also be considered that NPP trends were derived from a shorter record (2003–2023) than chl-*a* trends (1998–2025), excluding part of the 2023–2024 marine heatwave, which may also contribute to the discrepancies between both variables, particularly as seen within the PU region.

In this context, examining recent changes in upwelling-favourable winds is particularly relevant, as stronger winds may enhance coastal upwelling intensity [41,42,83,84]. Additionally, an intensification of wind-driven upwelling between 21°N and 25°N, corresponding to the PU subregion, despite the absence of a parallel increase in chl-*a* concentrations has been reported

[85]. They also described increases in both the intensity and duration of upwelling between 29°N and 35°N, which corresponds to part of the CJWPU and CGWPU regions.

Earlier studies also suggested an intensification of the Canary Upwelling System, and their work estimated a positive trend in the total upwelling velocity of approximately $+1.3 \times 10^{-6}$ m s$^{-1}$ over the last three decades [86]. In contrast, more recent projections indicate an increase in water-column stratification across the upwelling regions extending from the Strait of Gibraltar to Cape Juby by the end of the century, potentially leading to a weakening of upwelling in this sector [87]. Their simulations further suggest stronger summer winds in the northern SU region, while enhanced stratification in the African upwelling system in CGWPU and CJWPU all year long.

In the present study, significant increases in upwelling-favourable winds were detected only in the PU and CJWPU regions (Table 2). These results suggest an intensification of the upwelling system, provided that the enhanced wind forcing is not offset by increasing stratification associated with ocean warming. Nevertheless, according to the results presented here, this potential enhancement of coastal upwelling is not reflected in the chl-*a* trends. On the contrary, the upwelling regions exhibit some of the strongest declines in surface chl-*a* concentrations.

Comparison of the upwelling-favourable wind stress trends obtained in this study with previous estimates reveals substantial agreement [19]. Similar magnitudes were obtained here (+18.23 mN m$^{-2}$ century$^{-1}$ for PU and +25.51 mN m$^{-2}$ century$^{-1}$ for CJWPU), while previous studies reported positive and significant trends across all upwelling regions, with stronger increases at higher latitudes [19]. Positive trends in wind intensity over the permanent upwelling areas have also been documented [37,41,88].

Despite these similarities, contrasting results have also been reported. Decreases in wind intensity have been identified both in the SU subregion and in the permanent upwelling regions [39,63,89]. These discrepancies are likely related to the high natural variability of wind fields, as well as differences in the datasets employed, the temporal periods analyzed, and the methodologies applied.

## 4 Conclusions

The NASE region experienced significant environmental changes during the study period, characterized by widespread ocean warming and predominantly negative productivity trends. Sea surface temperature (SST) increased across all subregions, with an overall increase of +2.58 °C century$^{-1}$, and with the strongest warming occurring in the open ocean, particularly around the Azores, where the mean trend reached +3.18 °C century$^{-1}$. In contrast, coastal upwelling areas showed comparatively weaker warming rates, with the permanent upwelling region (PU) exhibiting the lowest warming trend of +1.37 °C century$^{-1}$. This relative attenuation of warming may partially buffer these regions against some of the impacts of climate change.

The strongest biological changes were observed within the Northwest African upwelling system, where chlorophyll-*a* concentration, productive area, and, in most cases, net primary

production declined over time. The most pronounced decrease in chlorophyll-*a* concentration was detected in the permanent upwelling region, reaching −1.62 mg $m^{-3}$ $century^{-1}$, accompanied by a loss of -6.25% of productive area per century. These results suggest a reduction in the productive capacity of some of the most important ecosystems in the region. In contrast, several oceanic and island-associated areas exhibited weak positive trends in chlorophyll-*a* or NPP, highlighting the spatial complexity of ecosystem responses to climate forcing.

Although upwelling-favourable winds intensified up to +15.98 mN $m^{-2}$ $century^{-1}$ in parts of the Canary Upwelling System, this was not accompanied by increases in chlorophyll concentration, indicating that stronger wind forcing may be partially offset by warming-induced stratification and other environmental changes. Finally, the inclusion of data up to 2025 strengthened several trend estimates and highlighted the influence of the exceptional 2023–2024 North Atlantic marine heatwave, suggesting that recent environmental changes may be increasingly shaped by extreme climatic events. Overall, this study shows how the inclusion of the most recent and exceptionally warm years can affect estimates of previously reported regional trends, while a finer spatial subdivision reveals contrasting physical and biological responses between open-ocean waters, waters surrounding the islands, and coastal upwelling systems.

## 5 Methodology

### 5.1 Study Area

The study area corresponds to the NASE region (20°N–45°N; 30°W–5°W, see Figure 1 and Table 1). This area was proposed by Siemer et al. (2021) [19], thus facilitating comparability and reproducibility of the study. To assess the impact of climate change on different areas of interest, seventeen subregions (boxes) are analysed for oceanic climate trends, including some in the open ocean and others in coastal upwelling zones: four in the Azores (AZ1–AZ4), two in Madeira (MA1–MA2), three in the Canary Islands (CI1–CI3), three sectors of the northwest African upwelling system (Cape Ghir Weak Permanent Upwelling, CGWPU; Cape Juby Weak Permanent Upwelling, CJWPU; Permanent Upwelling, PU), one seasonal upwelling region off the Iberian Peninsula (SU), and one open-ocean region (OR). The larger AZ, MA and CI domains are retained to provide greater regional context. These new boxes allow a better isolation of localized dynamics, and may

help to capture the effect of mesoscale processes that are not resolved when averaging over larger boxes.

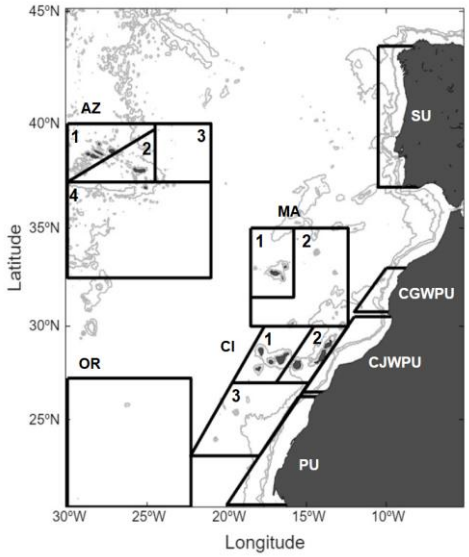



**Figure 1.** Map of the Eastern North Atlantic subtropical gyre (NASE) with areas of interest indicated by polygons. Four polygons are located in upwelling areas: the Permanent Upwelling area (PU), Cape Juby Weak Permanent Upwelling area (CJWPU), Cape Ghir Weak Permanent Upwelling area (CGWPU), and the Seasonal Upwelling area (SU). Four polygons in the open ocean represent the Canary Islands area (CI, CI1-CI3), the Oceanic Region (OR), the Azores archipelago (AZ, AZ1-AZ4) and the Madeira Islands (MA, MA1-MA2).

The Azores (AZ) area was further subdivided into several subregions to better resolve spatial variability. These include the central island group (AZ1) and the western island group (AZ2). In addition, the eastern sector (AZ3) and the southern sector (AZ4) were analysed to explore potential differences in climate-related signals across the archipelago and its surrounding waters.

The Madeira region (MA) was divided into MA1, encompassing the waters immediately surrounding the main islands, and MA2, representing the wider surrounding ocean. This distinction allows local conditions around the islands to be compared with those in the surrounding open ocean.

The Canary Islands region (CI) was subdivided into two groups of islands (CI1 and CI2) and a southern sector (CI3) located downstream of the archipelago. CI3 was selected because it may be influenced by island wakes, eddies and upwelling filaments originating from the Northwest

African coast [90]. Thus, this subdivision allows the comparison of waters surrounding the islands with the downstream oceanic region potentially affected by these processes.

An open-ocean region (OR) was selected to study the oligotrophic conditions away from coast and archipelagos.

EBUS areas were selected according to their intensity and seasonal behaviour following a previously established classification based on the references cited therein [19].

### 5.2 SST

Sea surface temperature (SST) data were provided by the National Oceanic and Atmospheric Administration (NOAA), combining satellite data (AVHRR) with *in situ* measurements from the International Ocean-Atmosphere Data Set (ICOADS) through interpolation (https://www.ncei.noaa.gov/access/search/datasets/sea-surface-temperature-optimum-interpolation/), with a spatial resolution of 0.25° x 0.25° and a daily temporal resolution. Data were downloaded from January 1, 1982, to December 31, 2025.

### 5.3 Chl-*a*

Chlorophyll-*a* data were obtained from the Copernicus Marine Environmental Monitoring Service (CMEMS). For the Global Ocean Satellite Observations, Bio-Geo-Chemical (BGC) products are provided by ACRI-ST (Sophia Antipolis, France) and are generated using the Copernicus-GlobColour processing chain. These products combine observations from multiple satellite sensors, including SeaWiFS, MODIS, MERIS, VIIRS-SNPP & JPSS1, and OLCI-S3A & S3B for the multi-sensor products, and OLCI-S3A & S3B only for the OLCI products. This database has been used in previous trend analyses and has shown robust performance when compared with independent datasets [21].

The chlorophyll-*a* mass concentration in surface waters is derived through a space–time interpolation procedure that provides a cloud-free product. The dataset has a daily temporal resolution and an original spatial resolution of 4 × 4 km, and was regridded to a regular 0.25° × 0.25° grid for processing with linear interpolation. The time series spans from January 1, 1998 to December 31, 2025.

For the EBUS regions, a productive area is defined as the total area with chlorophyll-*a* concentrations greater than 2 mg $m^{-3}$ [91]. For the open-ocean regions, unproductive (oceanic desert) areas were defined as those with chlorophyll-*a* concentrations lower than 0.07 mg $m^{-3}$ and calculated using the same approach. In addition, trends in the annual number of days exceeding these thresholds were evaluated: days with chlorophyll-*a* > 2 mg $m^{-3}$ in upwelling regions and days with chlorophyll-*a* < 0.07 mg $m^{-3}$ in oceanic regions.

### 5.4 NPP

Net primary production (NPP) data were obtained from the carbon-based production model (CbPM) provided by Oregon State University (http://orca.science.oregonstate.edu/).

Unlike chlorophyll-based models, the CbPM estimates NPP from phytoplankton carbon, accounting for the physiological state of primary producers. Phytoplankton carbon is derived from an empirical relationship with the particulate backscattering coefficient, while growth rates are estimated from chlorophyll-to-carbon ratios. NPP is subsequently calculated from phytoplankton carbon and growth rate [17,92].

MODIS-derived CbPM data were used, as they provide NPP trends with the highest statistical significance in the Canary Upwelling System [51]. The dataset has a monthly temporal resolution and a native spatial resolution of 1/12°, which was regridded to 0.25° using linear interpolation to match the SST and chlorophyll-*a* products. The time series spans from January 1, 2003 to December 31, 2023.

### 5.5 Wind

Wind data were obtained from the ERA5 reanalysis product. The dataset consists of zonal and meridional wind components at 10 m above the surface, with daily temporal resolution and a spatial resolution of 0.25° × 0.25°. The time series spans from January 1, 1992 to December 31, 2025.

From the zonal and meridional wind components, zonal and meridional wind stress intensities ($\tau_x$ and $\tau_y$) were calculated as follows

$$\tau_x=\rho_a C_d\sqrt{u^2+v^2}u \text{ and } \tau_y=\rho_a C_d\sqrt{u^2+v^2}v \quad (1)$$

where $\rho_a$ is the air density (1.22 kg $m^{-3}$), $C_d$ the dimensionless drag coefficient, in this case, 1.3 × $10^{-3}$ [93], and $u$, $v$ are the zonal and meridional component of wind (m $s^{-1}$), respectively. In the permanent upwelling regions, the meridional wind stress was rotated clockwise by the prevailing wind angle to obtain the component most favourable for upwelling as shown in equation (2) in order to calculate the mean trends for each region.

$$\tau'_y=\tau_x sin(\theta)+\tau_y cos(\theta) \quad (2)$$

where θ is the clockwise rotation angle between the original geographic coordinate system (east–north) and the rotated reference frame aligned with the upwelling-favourable wind direction. This approach assumes that, in a permanent upwelling system, the predominant wind direction (see Figure 5a) corresponds to the orientation that most effectively promotes upwelling (PU: 60°; CJWPU: 75.5°; CGWPU: 65°; CI: 40°, measured clockwise). Since the strictly meridional direction of the wind is the most favourable to the upwelling formation in SU, the wind was not rotated for that subregion (Figure 5a). Furthermore, for all of the upwelling areas, as wind forcing in upwelling regions is predominantly equatorward throughout the year, the full meridional wind stress dataset was considered.

### 5.6 Calculation of Trends

Except for the annual number of productive/unproductive days, seasonal annual variability was eliminated by calculating the mean value for each day of the year and for each grid point. The resulting mean annual cycle was then subtracted from the observed data at each pixel to obtain anomalies.

From these anomalies, trends and p-values were calculated using Matlab R2025b *regress* linear regression function [94] for SST, productive/unproductive area, NPP, meridional and zonal wind stress. For surface chlorophyll concentration and the annual number of productive/unproductive days, robust linear regression function *robustfit* [95,96] was used to reduce the influence of outliers and non-Gaussian distributions. Statistical significance was assessed at the 95 % confidence level for both methods.

## References

[1] McKay, D. I. A. et al. Exceeding 1.5°C global warming could trigger multiple climate tipping points. *Science.* **377**, eabn7950; https://doi.org/10.1126/science.abn7950 (2022).

[2] IPCC (2023). Climate Change 2023: Synthesis Report. Contribution of Working Groups I, II and III to the Sixth Assessment Report of the Intergovernmental Panel on Climate Change [ H. Lee and J. Romero (eds.)]. IPCC. https://doi.org/10.59327/IPCC/AR6-9789291691647.

[3] Copernicus Climate Change Service. The 2024 annual climate summary: Global climate highlights 2024. https://climate.copernicus.eu/global-climate-highlights-2024 (2024).

[4] Cheng, L., Abraham, J., Hausfather, Z., & Trenberth, K. E. How fast are the oceans warming? *Science*, **363**, 128-129; https://doi.org/10.1126/science.aav7619 (2019).

[5] Church, J. A., & White, N. J. Sea-Level Rise from the Late 19th to the Early 21st Century. *Surv. Geophys.*, **32**, 585–602; https://doi.org/10.1007/s10712-011-9119-1 (2011).

[6] Hansen, J., Sato, M., Kharecha, P., & Von Schuckmann, K. Atmospheric Chemistry and Physics Earth's energy imbalance and implications. *Atmos. Chem. Phys.* **11**, 13421–13449; https://doi.org/10.5194/acp-11-13421-2011 (2011).

[7] Levitus, S. et al. World ocean heat content and thermosteric sea level change (0-2000m), 1955-2010. *Geophy. Res. Lett.* **39**, L10603; https://doi.org/10.1029/2012GL051106 (2012).

[8] Liang, T. Y., Hsiao, S. C., Wu, H. L., Chen, H., & Chen, W. B. Accelerated Ocean thermal expansion and its contribution to Global Sea-level rise. *J. Sea Res*. **205**, 102589; https://doi.org/10.1016/J.SEARES.2025.102589 (2025).

[9] Gouretski, V., & Koltermann, K. P. How much is the ocean really warming? *Geophys. Res. Lett.* **34**, L01610; https://doi.org/10.1029/2006GL027834 (2007).

[10] Johnson, G. C., & Lyman, J. M. Warming trends increasingly dominate global ocean. *Nat. Clim. Chang.* **10**, 757–761; https://doi.org/10.1038/s41558-020-0822-0 (2020).

[11] Levitus, S., Antonov, J., & Boyer, T. Warming of the world ocean, 1955-2003. *Geophys. Res. Lett.* **32**, L02604; https://doi.org/10.1029/2004GL021592 (2005).

[12] Doney, S. C. Plankton in a warmer world. *Nature.* **444**, 695–696; https://doi.org/10.1038/444695a (2006).

[13] Frölicher, T. L., Fischer, E. M., & Gruber, N. Marine heatwaves under global warming. *Nature.* **560**, 360–364; https://doi.org/10.1038/s41586-018-0383-9 (2018).

[14] Parmesan, C. Ecological and evolutionary responses to recent climate change. *Annu. Rev. Ecol. Evol. Syst.* **37**, 637–669; https://doi.org/10.1146/annurev.ecolsys.37.091305.110100 (2006).

[15] Tuchen, F. P., Perez, R. C., Foltz, G. R., McPhaden, M. J., & Lumpkin, R. Strengthening of the Equatorial Pacific Upper-Ocean Circulation Over the Past Three Decades. *J. Geophys. Res. Oceans*. **129**, e2024JC021343; https://doi.org/10.1029/2024JC021343 (2024).

[16] Zhao, M., & Knutson, T. Crucial role of sea surface temperature warming patterns in near-term high-impact weather and climate projection. *Npj Clim. Atmos. Sci.* **7**, 130; https://doi.org/10.1038/s41612-024-00681-7 (2024).

[17] Behrenfeld, M. J. et al. Climate-driven trends in contemporary ocean productivity. *Nature*, **444**, 752–755; https://doi.org/10.1038/nature05317 (2006).

[18] Boyce, D. G., Lewis, M. R., & Worm, B. Global phytoplankton decline over the past century. *Nature.* **466**,591–596; https://doi.org/10.1038/nature09268 (2010).

[19] Siemer, J. P. et al. Recent Trends in SST, Chl-a, Productivity and Wind Stress in Upwelling and Open Ocean Areas in the Upper Eastern North Atlantic Subtropical Gyre. *J. Geophys. Res. Oceans*. **126**, e2021JC017268; https://doi.org/10.1029/2021JC017268 (2021).

[20] Signorini, S. R., Franz, B. A., & McClain, C. R. Chlorophyll variability in the oligotrophic gyres: Mechanisms, seasonality and trends. *Front. Mar. Sci.* **2**, 127882; https://doi.org/10.3389/FMARS.2015.00001/BIBTEX (2015).

[21] Tian, F., & Zhang, R. H. Emerging Hotspots of Surface Chlorophyll Trend in the Tropical Oceans. *J. Geophys. Res. Oceans*. **129**, e2023JC020681; https://doi.org/10.1029/2023JC020681 (2024).

[22] Calbet, A., & Landry, M. R. Phytoplankton growth, microzooplankton grazing, and carbon cycling in marine systems. *Limnol. Oceanogr*. **49**, 51–57; https://doi.org/10.4319/LO.2004.49.1.0051 (2004).

[23] Falkowski, P. G. The role of phytoplankton photosynthesis in global biogeochemical cycles. *Photosynth. Res.* **39**, 235–258; https://doi.org/10.1007/BF00014586 (1994).

[24] Field, C. B., Behrenfeld, M. J., Randerson, J. T., & Falkowski, P. Primary production of the biosphere: Integrating terrestrial and oceanic components. *Science.* **281**, 237–240; https://doi.org/10.1126/science.281.5374.237 (1998).

[25] Blanchard, J. L. et al. Potential consequences of climate change for primary production and fish production in large marine ecosystems. *Philos. Trans. R. Soc. Lond. B Biol. Sci*. **367**, 2979–2989. https://doi.org/10.1098/RSTB.2012.0231 (2012).

[26] Silsbe, G. M., Fox, J., Westberry, T. K., & Halsey, K. H. Global declines in net primary production in the ocean color era. *Nat. Commun.* **16**, 5821; https://doi.org/10.1038/s41467-025-60906-y (2025).

[27] Yang, K., Meyer, A., Strutton, P. G., & Fischer, A. M. Global trends of fronts and chlorophyll in a warming ocean. *Commun. Earth Environ*. **4**, 489; https://doi.org/10.1038/s43247-023-01160-2 (2023).

[28] Marañón, E. Phytoplankton growth rates in the Atlantic subtropical gyres. *Limnol. Oceanogr.* **50**, 299–310; https://doi.org/10.4319/LO.2005.50.1.0299 (2005).

[29] McClain, C. R., Signorini, S. R., & Christian, J. R. Subtropical gyre variability observed by ocean-color satellites. *Deep Sea Res. Part II Top. Stud. Oceanogr*. **51**, 281–301; https://doi.org/10.1016/J.DSR2.2003.08.002 (2004).

[30] Signorini, S. R., & McClain, C. R. Subtropical gyre variability as seen from satellites. *Remote Sens. Lett*. **3**, 471–479; https://doi.org/10.1080/01431161.2011.625053 (2012).

[31] Huang, R. X., & Russell, S. Ventilation of the Subtropical North Pacific. *J. Phys. Oceanogr*. **24**, 2589–2605; https://doi.org/10.1175/1520-0485(1994)024%3C2589:VOTSNP%3E2.0.CO;2 (1994).

[32] Munk, W. H. On the wind-driven ocean circulation. *J. Meteorol*. **7**, 79–93; https://doi.org/10.1175/1520-0469(1950)007%3C0080:OTWDOC%3E2.0.CO;2 (1950).

[33] Huang, R., Zhang, X., Church, J. A., & Hu, J. Asymmetric Changes of the Subtropical Gyre Circulation and Associated Sea Level Over 1960–2018 in the Pacific Ocean. *J. Geophys. Res. Oceans*. **130**, e2024JC021785; https://doi.org/10.1029/2024JC021785 (2025).

[34] Gregg, W. W., Casey, N. W., & McClain, C. R. Recent trends in global ocean chlorophyll. *Geophys. Res. Lett*. **32**, L03606; https://doi.org/10.1029/2004GL021808 (2005).

[35] Vantrepotte, V., & Mélin, F. Temporal variability of 10-year global SeaWiFS time-series of phytoplankton chlorophyll a concentration. *ICES J. Mar. Sci.* **66**, 1547–1556; https://doi.org/10.1093/icesjms/fsp107 (2009).

[36] Vantrepotte, V., & Mélin, F. Inter-annual variations in the SeaWiFS global chlorophyll a concentration (1997-2007). *Deep Sea Res. Part I Oceanogr. Res. Pap.* **58**, 429–441; https://doi.org/10.1016/j.dsr.2011.02.003 (2011).

[37] Cropper, T. E., Hanna, E., & Bigg, G. R. Spatial and temporal seasonal trends in coastal upwelling off Northwest Africa, 1981–2012. *Deep Sea Res. Part I Oceanogr. Res. Pap*. **86**, 94–111; https://doi.org/10.1016/J.DSR.2014.01.007 (2014).

[38] Pauly, D., & Christensen, V. Primary production required to sustain global fisheries. *Nature.* **374**, 255–257; https://doi.org/10.1038/374255A0 (1995).

[39] Demarcq, H. Trends in primary production, sea surface temperature and wind in upwelling systems (1998-2007). *Prog. Oceanogr.* **83**, 376–385; https://doi.org/10.1016/j.pocean.2009.07.022 (2009).

[40] Seabra, R. et al. Reduced nearshore warming associated with eastern boundary upwelling systems. Front. Mar. Sci. **6**, 104; https://doi.org/10.3389/FMARS.2019.00104 (2019).

[41] Bakun, A. Global Climate Change and Intensification of Coastal Ocean Upwelling. *Science*. **247**, 198-201; https://doi.org/10.1126/science.247.4939.198 (1990).

[42] García-Reyes, M. et al. Under pressure: Climate change, upwelling, and eastern boundary upwelling ecosystems. *Front. Mar. Sci*. **2**, 109; https://doi.org/10.3389/FMARS.2015.00109 (2015).

[43] Lopes, J. F., Ferreira, J. A., Cardoso, A. C., & Rocha, A. C. Variability of temperature and chlorophyll of the Iberian Peninsula near costal ecosystem during an upwelling event for the

present climate and a future climate scenario. *J. Mar. Syst*. **129**, 271–288; https://doi.org/10.1016/J.JMARSYS.2013.07.002 (2014).

[44] Rykaczewski, R. R., Dunne, J. P., Sydeman, W. J., García-Reyes, M., Black, B. A., & Bograd, S. J. Poleward displacement of coastal upwelling-favorable winds in the ocean's eastern boundary currents through the 21st century. *Geophy. Res. Lett*. **42**, 6424–6431; https://doi.org/10.1002/2015GL064694 (2015).

[45] Sousa, M. C., Alvarez, I., deCastro, M., Gomez-Gesteira, M., & Dias, J. M. Seasonality of coastal upwelling trends under future warming scenarios along the southern limit of the canary upwelling system. *Prog. Oceanogr.* **153**, 16–23; https://doi.org/10.1016/J.POCEAN.2017.04.002 (2017).

[46] Sylla, A., Mignot, J., Capet, X., & Gaye, A. T. Weakening of the Senegalo–Mauritanian upwelling system under climate change. *Clim. Dyn*. **53**, 4447–4473; https://doi.org/10.1007/S00382-019-04797-Y (2019).

[47] Varela, R., Rodríguez-Díaz, L., de Castro, M., & Gómez-Gesteira, M. Influence of Canary upwelling system on coastal SST warming along the 21st century using CMIP6 GCMs. Glob. Planet. Change. **208**, 103692; https://doi.org/10.1016/J.GLOPLACHA.2021.103692 (2022).

[48] Falarz, M. Azores High and Hawaiian High: correlations, trends and shifts (1948–2018). *Theor. Appl. Climatol*. **138**, 417–431; https://doi.org/10.1007/s00704-019-02837-5 (2019).

[49] Cordeiro Pires, A., Nolasco, R., Rocha, A., Ramos, A. M., & Dubert, J. Climate change in the Iberian Upwelling System: a numerical study using GCM downscaling. *Clim. Dyn*. **47**, 451–464; https://doi.org/10.1007/S00382-015-2848-Y (2016).

[50] Miranda, P. M. A., Alves, J. M. R., & Serra, N. Climate change and upwelling: Response of Iberian upwelling to atmospheric forcing in a regional climate scenario. *Clim. Dyn.* **40**, 2813–2824; https://doi.org/10.1007/S00382-012-1442-9 (2013).

[51] Gómez-Letona, M., Ramos, A. G., Coca, J., & Arístegui, J. Trends in primary production in the canary current upwelling system-A regional perspective comparing remote sensing models. *Front. Mar. Sci*. **4**, 370; https://doi.org/10.3389/FMARS.2017.00370 (2017).

[52] Tim, N., Zorita, E., Hünicke, B., Yi, X., & Emeis, K. C. The importance of external climate forcing for the variability and trends of coastal upwelling in past and future climate. Ocean Sci. **12**, 807–823; https://doi.org/10.5194/OS-12-807-2016 (2016).

[53] England, M.H. et al. Drivers of the extreme North Atlantic marine heatwave during 2023. *Nature.* **642**, 636–643; https://doi.org/10.1038/s41586-025-08903-5 (2025).

[54] Ferreira, T. M., Trigo, R. M., Gaspar, T. H., Pinto, J. G., & Ramos, A. M. The record-breaking precipitation event of December 2022 in Portugal. *Nat. Hazards Earth Syst. Sci.* **25**, 609–623; https://doi.org/10.5194/nhess-25-609-2025 (2025).

[55] Guinaldo, T., Cassou, C., Sallée, J.B., & Liné, A. Internal variability effect doped by climate change drove the 2023 marine heat extreme in the North Atlantic. *Commun. Earth Environ*. **6**, 291; https://doi.org/10.1038/s43247-025-02197-1 (2025).

[56] Saurral, R. I. et al. The key role of Mediterranean and North Atlantic sea surface temperatures on the 2024 record-breaking Valencia precipitation event. *Weather Clim. Extrem.* **52**, 100877; https://doi.org/10.1016/j.wace.2026.100877 (2026).

[57] Caruso, S. et al. Three Decades of Environmental Change in European Macaronesia: Long-Term Trends, Vertical Gradients, and Multi-Trophic Ecosystem Responses. Preprint at https://dx.doi.org/10.2139/ssrn.6571474 (2026).

[58] Casey, K. S., & Cornillon, P. Global and regional sea surface temperature trends. *J. Clim.* **14**, 3801–3818; https://doi.org/10.1175/1520-0442(2001)014<3801:GARSST>2.0.CO;2 (2001).

[59] Karnauskas, K.B., Zhang, L., & Amaya, D.J. The Atmospheric Response to North Atlantic SST Trends, 1870–2019. *Geophy. Res. Lett.* **48**, e2020GL090677; https://doi.org/10.1029/2020GL090677 (2020).

[60] Machín, F., Aguirre, C., Veitch, J., García-Reyes, M., Kämpf, J. One hundred years of progress in understanding the dynamics of Eastern Boundary Upwelling Systems. ICES J. Mar. Sci. **83**, fsag107; https://doi.org/10.1093/icesjms/fsag107 (2026).

[61] Kessler, A., Goris, N., Lauvset, S.K. Observation-based Sea surface temperature trends in Atlantic large marine ecosystems. *Prog. Oceanogr*. **208**, 102902; https://doi.org/10.1016/j.pocean.2022.102902 (2022).

[62] Baptista, V., Silva, P. L., Relvas, P., & Teodósio, M. A. Sea surface temperature variability along the Portuguese coast since 1950. *Int. J. Climatol*. **38**, 1145–1160; https://doi.org/10.1002/joc.5231 (2017).

[63] Pardo, P. C., Padín, X. A., Gilcoto, M., Farina-busto, L., & Pérez, F. F. Evolution of upwelling systems coupled to the long-term variability in sea surface temperature and Ekman transport. *Clim. Res*. **48**, 231–246; https://doi.org/10.3354/cr00989 (2011).

[64] Davis, R. E., Hayden, B. P., Gay, D. A., Phillips, W. L., & Jones, G. V. The North Atlantic Subtropical Anticyclone. *J. Clim.* **10**, 728-744; https://doi.org/10.1175/1520-0442(1997)010<0728:TNASA>2.0.CO;2 (1997).

[65] Madruga, J., Azevedo, E. B., Sampaio, J. F., Fernandes, F., Reis, F., & Pinheiro, J. Analysis and definition of potential new areas for viticulture in the Azores (Portugal). *SOIL*. **1**, 515–526; https://doi.org/10.5194/soil-1-515-2015 (2015).

[66] Azorin-Molina, C. et al. Wind speed variability over the Canary Islands, 1948–2014: focusing on trend differences at the land–ocean interface and below–above the trade-wind inversion layer. *Clim Dyn*, **50**, 4061–4081; https://doi.org/10.1007/s00382-017-3861-0 (2018).

[67] Portalés-Julià, P., & Machín, F. Long-term changes in air-sea heat fluxes in the North Atlantic: Toward a latitudinal reorganization of the ocean heat budget. *J. Sea Res.* **210**, 102688; https://doi.org/10.1016/j.seares.2026.102688 (2026).

[68] Belkin, I. M. Rapid warming of large marine ecosystems. *Prog. Oceanogr*. **81**, 207–213; https://doi.org/10.1016/j.pocean.2009.04.011 (2009).

[69] Garcia-Soto, C. et al. An Overview of Ocean Climate Change Indicators: Sea Surface Temperature, Ocean Heat Content, Ocean pH, Dissolved Oxygen Concentration, Arctic Sea Ice Extent, Thickness and Volume, Sea Level and Strength of the AMOC (Atlantic Meridional Overturning Circulation). *Front. Mar. Sci.* **8**, 642372; https://doi.org/10.3389/fmars.2021.642372 (2001).

[70] Chang, M.-H., Huang, Y.-C., Cheng, Y.-H., Terng, C.-T., Chen, J., & Jan, J.C. Revisiting regression methods for estimating long-term trends in sea surface temperature. *Nat. Hazards Earth Syst. Sci.* **24**, 2481–2494; https://doi.org/10.5194/nhess-24-2481-2024 (2024).

[71] Cheng, L., Foster, G., Hausfather, Z., Trenberth, K. E., & Abraham, J. Improved Quantification of the Rate of Ocean Warming. *J. Clim*. **35**, 4827-4840; https://doi.org/10.1175/JCLI-D-21-0895.1 (2022).

[72] Zhang, M. et al. Long-term ocean temperature trend and marine heatwaves. *J. Ocean. Limnol*. **42**, 1037–1047; https://doi.org/10.1007/s00343-023-3160-z (2024).

[73] Alonso-Perez, S. et al. Trend changes of African airmass intrusions in the marine boundary layer over the subtropical Eastern North Atlantic region in winter. *Tellus B: Chem. Phys. Meteorol.* **63**, 255–265; https://doi.org/10.1111/j.1600-0889.2011.00524.x (2011).

[74] Suárez-Molina D, Cuevas E, Alonso-Pérez S, Cana L, Montenegro G., & Oliver A. Dust events characterization from visibility, trends and Dust Adversity Index in the Canary Islands for the period 1980–2022. *Heliyon.* 10, e31262; https://doi.org/10.1016/j.heliyon.2024.e31262 (2024).

[75] Behrenfeld, M. J., Boss, E., Siegel, D. A., & Shea, D. M. Carbon-based ocean productivity and phytoplankton physiology from space. *Global Biogeochem. Cycles.* **19**, GB1006; https://doi.org/10.1029/2004GB002299 (2005).

[76] Cloern, J.E., Grenz, C., & Vidergar-Lucas, L. An empirical model of the phytoplankton chlorophyll : carbon ratio-the conversion factor between productivity and growth rate. *Limnol. Oceanogr.* **40**, 1313-1321; https://doi.org/10.4319/lo.1995.40.7.1313 (1995).

[77] Geider, R.J., MacIntyre, H.L., & Kana, T.M. Dynamic model of phytoplankton growth and acclimation: responses of the balanced growth rate and the chlorophyll a: carbon ratio to light, nutrient-limitation and temperature. *Mar. Ecol. Prog. Ser*. **148**, 187-200; https://doi.org/10.3354/meps148187 (1997).

[78] Graff, J.R. et al. Photoacclimation of natural phytoplankton communities. *Mar. Ecol. Prog. Ser*. **542**, 51-62; https://doi.org/10.3354/meps11539 (2016).

[79] Sasai, Y., Smith, S. L., Siswanto, E., Sasaki, H., & Nonaka, M. Physiological flexibility of phytoplankton impacts modelled chlorophyll and primary production across the North Pacific Ocean. *Biogeosciences.* **19**, 4865–4882; https://doi.org/10.5194/bg-19-4865-2022 (2022).

[80] Zonneveld, C. A cell-based model for the chlorophyll a to carbon ratio in phytoplankton. *Ecol. Model*. **113**, 55-70; https://doi.org/10.1016/S0304-3800(98)00134-3 (1998).

[81] Marañón, E., Behrenfled, M.J., González, N., Mouriño, B., Zubkov, M.V. High variability of primary production in oligotrophic waters of the Atlantic Ocean: uncoupling from phytoplankton biomass and size structure. *Mar. Ecol. Prog. Ser*. **257**, 1-11; https://doi.org/10.3354/meps257001 (2003).

[82] Moreno-Ostos, E. et al. Size-fractionated phytoplankton biomass and production in the tropical Atlantic. *Sci. Mar*. **75**, 379-8; https://doi.org/10.3989/scimar.2011.75n2379 (2011).

[83] Bakun, A., Field, D.B., Redondo-Rodríguez, A., & Weeks, S.J. Greenhouse gas, upwelling-favorable winds, and the future of coastal ocean upwelling ecosystems. *Glob. Change Biol*. **16**, 1213-1228; https://doi.org/10.1111/j.1365-2486.2009.02094.x (2010).

[84] Sydeman, W.J. et al. Climate change and wind intensification in coastal upwelling ecosystems. *Science.* **345**, 77-80; https://doi.org/10.1126/science.1251635 (2014).

[85] Cabrera-Busto, J., Ramírez-Romero, E., Buttay, L., & Llope, M. Regionalization and Multidecadal Change in the Southern Canary Current Large Marine Ecosystem. *J. Geophys. Res. Oceans*. **131**, e2025JC023075; https://doi.org/10.1029/2025JC023075 (2026).

[86] Polonsky, A. B., & Serebrennikov, A. N. Intensification of Atlantic and Pacific Large-Scale Upwelling under Recent Climate Conditions. *Dokl. Earth Sc.* **492**, 480–484. https://doi.org/10.1134/S1028334X20060161 (2020).

[87] Vázquez, R. et al. Climate change in the Canary/Iberia upwelling region: The role of ocean stratification and wind. *Environ. Res. Lett*. **19**, 074064; https://doi.org/10.1088/1748-9326/ad5ab4 (2024).

[88] McGregor, H. V., Fischer, H. W., & Mulitza, S. Rapid 20th-Century Increase in Coastal Upwelling off Northwest Africa. *Science.* **315**, 637-639; https://doi.org/10.1126/science.1134839 (2007).

[89] Barton, E. D., Field, D. B., & Roy, C. Canary current upwelling: More or less? *Prog. Oceanogr.* **116**, 167–178; https://doi.org/10.1016/j.pocean.2013.07.007 (2013).

[90] Fraile-Nuez, E., & Hernández-Guerra, A. Wind-driven circulation for the eastern North Atlantic Subtropical Gyre from Argo data. *Geophys. Res. Lett.* **33**, L03601; https://doi.org/10.1029/2005gl025122 (2006).

[91] Polovina, J. J., Howell, E. A., & Abecassis, M. Ocean's least productive waters are expanding. *Geophys. Res. Lett*. **35**, L03618; https://doi.org/10.1029/2007GL031745 (2008).

[92] Westberry, T., Behrenfeld, M. J., Siegel, D. A., & Boss, E. Carbon-based primary productivity modeling with vertically resolved photoacclimation. *Global Biogeochem. Cycles.* **22**, GB2024; https://doi.org/10.1029/2007GB003078 (2008).

[93] Schwing, F.B., Farrell, M.O., Steger, J.M., & Baltz, K. Coastal Upwelling Indices WestCoast of North America 1946-95 (NOAA Technical Memorandum NMFS-SWFSC-231). National Marine Fisheries Service, Southwest Fisheries Science Center. https://repository.library.noaa.gov/ (1996).

[94] Chatterjee, S., & Hadi, A. S. Influential observations, high leverage points, and outliers in linear regression. *Stat. Sci*. **1**, 379–393; https://doi.org/10.2307/224613410.1214/ss/1177013630 (1986).

[95] DuMouchel, W. H. & O'Brien, F. L. Integrating a robust option into a multiple regression computing environment. *Computer Science and Statistics: Proceedings of the 21st Symposium on the Interface.* 297–301 (American Statistical Association, Alexandria, VA, 1989).

[96] Holland, P. W., Welsch, R. E. Robust regression using iteratively reweighted least-squares. *Commun. Stat. - Theory Methods.* **6**, 813–827; https://doi.org/10.1080/03610927708827533 (1997).

## Acknowledgments

This research was funded through the Promotur Turismo Canarias Agreement for the joint implementation of initiatives aimed at intelligent management and the development of the Blue Tourism product. These efforts fall within the framework of the Recovery, Transformation, and Resilience Plan (Next Generation EU Funds) and align with Order No. 257/2023 issued by the Minister of Tourism and Employment, focused on the execution of cohesion actions in destinations as part of the Canary Islands Territorial Plan.

## Author contributions

C.P. conceptualized the study, developed the methodology, curated the data, performed the formal analyses, developed the software, prepared the visualizations, and wrote the original draft of the manuscript. A.G.-V. contributed to the methodology, formal analysis, validation, visualization, manuscript review and editing, supervision, and project administration. F.M. contributed to the methodology, formal analysis, validation, manuscript review and editing, and supervision. E.P.M. contributed to software development, validation, manuscript review and editing, and supervision. J.P.M.-D. contributed to formal analysis, manuscript review and editing, and supervision. S.A.-C. contributed to visualization, manuscript review and editing, and supervision. E.F.-N. conceived the study, contributed to the methodology, formal analysis and software development, reviewed and edited the manuscript, supervised the research, managed the project, acquired funding, and served as the corresponding author. All authors read and approved the final manuscript.

## Data Availability Statement

The data sets that were used for the analysis are publicly available and can be obtained from different institutions. The SST data can be obtained from NOAA (https://www.ncei.noaa.gov/access/search/datasets/sea-surface-temperature-optimum-interpolation/). The chl-*a* and the wind data were provided by Copernicus (https://resources.marine.copernicus.eu/). The NPP data are available at

http://orca.science.oregonstate.edu/ and is associated to the Oregon State University. The wind data was obtained from the ERA-5 reanalysis, provided by the Copernicus Climate Data Store (https://cds.climate.copernicus.eu/datasets/reanalysis-era5-single-levels-timeseries?tab=overview).

## Competing Interest Statement

The authors declare no competing interests.

## Figure Legends

**Figure 1.** Map of the Eastern North Atlantic subtropical gyre (NASE) with areas of interest indicated by polygons. Four polygons are located in upwelling areas: the Permanent Upwelling area (PU), Cape Juby Weak Permanent Upwelling area (CJWPU), Cape Ghir Weak Permanent Upwelling area (CGWPU), and the Seasonal Upwelling area (SU). Four polygons in the open ocean represent the Canary Islands area (CI, CI1-CI3), the Oceanic Region (OR), the Azores archipelago (AZ,AZ1-AZ4) and the Madeira Islands (MA, MA1-MA2).

**Figure 2.** (**a)** Spatial distribution of trends in sea surface temperature anomalies in the NASE region (1982–2025). Negative trends are shown in blue and near zero trends in white. The boundaries of each subregion are indicated. **(b)** Smoothed mean SST time series (366 days moving average) for each region. Trends were calculated from anomaly time series, to which the corresponding mean values were added back for visualization purposes only. Trends are separated into two plots for better visualization to avoid overlapping.

**Figure 3. (a)** Spatial distribution of trends in surface chlorophyll-*a* concentration anomalies in the NASE region (1998–2025). Negative trends are shown in blue and positive trends in green. The boundaries of each subregion are indicated. **(b)** Smoothed mean surface chl-*a* concentration time series (366 days moving average) for each subregion. Trends were calculated from anomaly time series to which the corresponding mean values were added back for visualization purposes only. Trends are separated into two plots for better visualization to avoid overlapping.

**Figure 4. (a)** Spatial distribution of trends in NPP anomalies in the NASE region (2003–2023). Negative trends are shown in blue and positive trends in orange. The boundaries of each subregion are indicated. **(b)** Smoothed mean NPP time series (12 months moving average) for each subregion. Trends were calculated from anomaly time series to which the corresponding mean values were added back for visualization purposes only. Trends are separated into two plots for better visualization to avoid overlapping.

**Figure 5. (a)** Spatial distribution of trends in meridional wind anomalies in the NASE region (1992–2025). Negative trends are shown in blue and positive trends in red. The boundaries of each subregion are indicated. Wind roses are added to display the average wind distribution in each

subregion. **(b)** Smoothed mean wind stress intensity time series (366 days moving average) for each subregion. In order to represent wind conditions most favourable for upwelling, data from CI, CGWPU, CJWPU, and PU were projected onto the dominant angle between wind direction and the meridional axis for each mentioned subregion. Trends were calculated from anomaly time series to which the corresponding mean values were added back for visualization purposes only. Trends are separated into two plots for better visualization to avoid overlapping.

## Tables

**Table 1.** Spatial extent of the defined subregions.

| Region | Acronym | Latitude (°N) | Longitude (°W) |
|---|---|---|---|
| Eastern North Atlantic subtropical gyre | NASE | 20 - 45 | 30 - 5 |
| Azores | AZ | 32.5 - 40 | 30 - 21 |
| | AZ1 | 37.25 - 40 | 30 - 24.5 |
| | AZ2 | 37.25 - 39.25 | 30 - 24.5 |
| | AZ3 | 37.25 - 40 | 24.5 - 21 |
| | AZ4 | 32.5 - 37.25 | 30 - 21 |
| Ocean Region | OR | 20 - 27.25 | 30 - 22.25 |
| Madeira | MA | 30 - 35 | 18.5 - 12.4 |
| | MA1 | 31.5 - 35 | 18.5 - 15.8 |
| | MA2 | 30 - 35 | 18.5 - 12.4 |
| Canary Islands | CI | 23 - 30 | 22.23 - 12.4 |
| | CI1 | 27 - 30 | 19.7 - 14.5 |
| | CI2 | 27 - 30 | 16.9 - 12.4 |
| | CI3 | 23 - 27 | 19.7 - 14.9 |
| Seasonal Upwelling | SU | 37 - 43.5 | 10.5 - 8 |
| Cape Ghir Weak Permanent Upwelling | CGWPU | 30.75 - 33 | 12 - 8 |
| Cape Juby Weak Permanent Upwelling | CJWPU | 26.5 - 30.5 | 15.25 - 9 |
| Permanent Upwelling | PU | 20.25 - 26.25 | 20.12 - 5 |

**Table 2**. Mean trends for SST, surface chl-*a* concentration, percentage of productive/unproductive area (EBUS and open ocean areas, respectively), NPP and wind stress intensity using temporal series ending in 2019 and in 2025. The non-significant values ($p > 0.05$) are marked with an asterisk.

| | SST (°C century$^{-1}$) | | Chl-*a* (mg m$^{-3}$ century$^{-1}$) | | Area (% century$^{-1}$) | | NPP (mg m$^{-2}$ day$^{-1}$ century$^{-1}$) | | Wind (mN m$^{-2}$ century$^{-1}$) | |
|---|---|---|---|---|---|---|---|---|---|---|
| | 1982-2019 | 1982-2025 | 1998-2019 | 1998-2025 | 1998-2019 | 1998-2025 | 2003-2019 | 2003-2023 | 1992-2019 | 1992-2025 |
| **NASE** | 2.08 | 2.58 | -0.02 | -0.13 | - | - | -126.74 | -74.69 | - | - |
| **AZ** | 2.77 | 3.18 | -0.02 | -0.06 | 11.36 | 16.98 | -305.88 | -162.12 | - | - |

| | | | | | | | | | | |
|---|---|---|---|---|---|---|---|---|---|---|
| **AZ1** | 2.57 | 2.95 | -0.01 | -0.06 | 8.68 | 6.40 | -297.79* | 25.36* | - | - |
| **AZ2** | 2.82 | 3.21 | 0.004* | -0.07 | 13.03 | 12.78 | -355.19 | -137.84* | - | - |
| **AZ3** | 2.78 | 3.39 | -0.03 | -0.10 | 11.66 | 26.29 | -267.96 | -136.83* | - | - |
| **AZ4** | 2.79 | 3.16 | -0.02 | -0.04 | 12.06 | 17.93 | -314.21 | -213.08 | - | - |
| **OR** | 1.67 | 2.22 | 0.02 | 0.03 | 8.32 | -17.59 | 225.57 | 178.85 | - | - |
| **MA** | 1.77 | 2.55 | 0.03 | -0.003* | -36.12 | -17.65 | -231.78 | -82.13* | - | - |
| **MA1** | 1.88 | 2.67 | 0.02 | -0.008 | -36.52 | -13.81 | -286.39 | -181.77 | - | - |
| **MA2** | 1.72 | 2.51 | 0.03 | -6.56e-7* | -37.13 | -20.47 | -204.04* | -37.86* | - | - |
| **CI** | 1.97 | 2.45 | 0.02 | 0.03 | -0.58* | -5.77 | -126.45* | 139.25* | 2.46* | -2.92* |
| **CI1** | 1.83 | 2.44 | 0.04 | 0.04 | -3.85* | -14.33 | -156.57* | 68.80* | -7.73 | -11.38 |
| **CI2** | 1.80 | 2.38 | 0.03 | -0.003 | 1.18 | 0.79 | -190.76* | 9.68* | 5.72 | 0.04* |
| **CI3** | 2.47 | 2.47 | 0.004* | 0.03 | 0.32* | -4.14 | -87.40* | 217.73 | 5.90 | -0.16* |
| **SU** | 1.53 | 2.02 | 0.27 | -0.2 | 2.98 | -0.10* | -423.15 | -351.38 | 10.06 | 2.70* |
| **CGWPU** | 0.9 | 1.40 | -0.03* | -0.08 | -1.98 | -0.63* | -913.33 | -232.85* | -0.61* | -0.96* |
| **CJWPU** | 1.52 | 1.86 | -0.28 | -0.35 | -3.91 | -3.16 | -894.14 | -459.56 | 15.32 | 12.32 |
| **PU** | 1.21 | 1.37 | -1.70 | -1.62 | -9.80 | -6.25 | 208.95 | 362.42 | 17.27 | 15.98 |